



Multiscale Parametrization Of a Friction Model For Metal Cutting Using Contact Mechanics, Atomistic Simulations, And Experiments

Hannes Holey^{1,2} · Florian Sauer³ · Prasanth Babu Ganta¹ · Leonhard Mayrhofer¹ · Martin Dienwiebel^{1,4} · Volker Schulze³ · Michael Moseler^{1,2,5}

Received: 1 July 2024 / Accepted: 10 August 2024
© The Author(s) 2024

Abstract

In this study, we developed and parametrized a friction model for finite element (FE) cutting simulations of AISI4140 steel, combining experimental data and numerical simulations at various scales. Given the severe thermomechanical loads during cutting, parametrization of friction models based on analogous experiments has been proven difficult, such that the cutting process itself is often used for calibration. Instead, our model is based on the real area of contact between rough surfaces and the stress required to shear adhesive micro contacts. We utilized microtextured cutting tools and their negative imprint on chips to orient chip and tool surfaces, enabling the determination of a combined surface roughness. This effective roughness was then applied in contact mechanics calculations using a penetration hardness model informed by indentation hardness measurements. Consistent with Bowden and Tabor theory, we observed that the fractional contact area increased linearly with the applied normal load, and the effective roughness remained insensitive to cutting fluid application. Additionally, we calculated the required shear stress as a function of normal load using DFT-based molecular dynamics simulations for a tribofilm formed at the interface, with its composition inferred from ex-situ XPS depth profiling of the cutting tools. Our friction model demonstrated good agreement with experimental results in two-dimensional FE chip forming simulations of orthogonal cutting processes, evaluated by means of cutting force, passive force, and contact length prediction. This work presents a proof of concept for a physics-based approach to calibrate constitutive models in metal cutting, potentially advancing the use of multiscale and multiphysical simulations in machining.

Hannes Holey and Florian Sauer contributed equally to this work.

✉ Hannes Holey
hannes.holey@unimi.it

✉ Florian Sauer
florian.sauer@kit.edu

✉ Michael Moseler
michael.moseler@iwm.fraunhofer.de

¹ MicroTribology Center μ TC, Fraunhofer Institute for Mechanics of Materials IWM, Wöhlerstr. 11, 79108 Freiburg, Germany

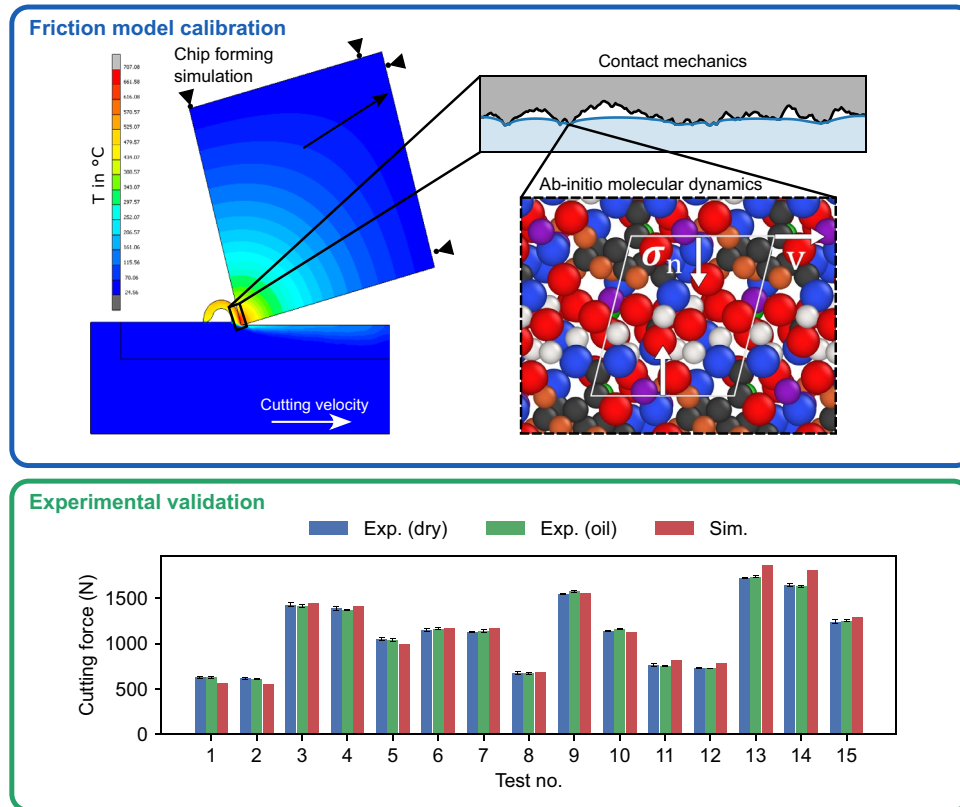
² Freiburg Materials Research Center, University of Freiburg, Stefan-Meier-Straße 21, 79104 Freiburg, Germany

³ wbk Institute of Production Science, Karlsruhe Institute of Technology (KIT), Kaiserstr. 12, 76131 Karlsruhe, Germany

⁴ Institute for Applied Materials (IAM-ZM), Karlsruhe Institute of Technology (KIT), Straße am Forum 7, 76131 Karlsruhe, Germany

⁵ Institute of Physics, University of Freiburg, Hermann-Herder-Straße 3, 79104 Freiburg, Germany

Graphical abstract



Keywords Friction models in metal cutting · Contact mechanics · Molecular dynamics

1 Introduction

Metal cutting plays an important role in today's manufacturing process chain for various engineering parts. This was enabled by immense research efforts to relate processing parameters to the properties of the produced part. Further optimization—in terms of both tool lifetime and product quality—of production processes requires an improved understanding of the mechanisms involved in cutting. Plasticity of the work material and friction at the tool chip interface predominantly determine the processing result. Thus, the success of finite element (FE) simulations in metal cutting to predict e.g. cutting forces and chip morphology hinges on an accurate description of the work material's plastic deformation and tool chip friction. The former is in most cases described with the Johnson-Cook [1] model accounting for rate dependence and thermal effects, whereas a variety of models have been used in the literature for the latter.

First attempts to relate chip tool friction to chip thickness relied on purely geometric considerations. Quick-stop

experiments in orthogonal cutting revealed that plastic flow occurs in a concentrated zone, the so-called primary shear zone [2]. In orthogonal cutting, simple trigonometric relations connect the orientation of the primary shear zone and the chip thickness (for a given rake angle and uncut chip thickness). Merchant [3] assumed that the angle formed by the shear zone will be such that it reduces the work done by the cutting force, which can be related to the tool chip friction with similar trigonometric arguments. Since cutting forces can be measured, this leads to a model that could theoretically predict chip formation based on friction.

Despite the failure of early analytical models [3, 4], more sophisticated theories of metal cutting based on similar ideas are still of research interest today [5, 6]. Interestingly, Merchant's model is equivalent to the Bowden and Tabor [7] theory of metal friction, which states that the friction coefficient is given by the ratio between the shear strength of the softer material and the normal pressure. The only difference between the models is the region where plastic flow occurs (within the primary shear zone or between micro contacts formed by the asperities of the contacting rough surfaces).

Today, it is well accepted, that there is no relation that captures both friction and plastic flow to uniquely describe cutting processes. Yet, more detailed investigations led to a better understanding of the energy dissipation in the bulk of the work material (plasticity) and at the interfaces (friction). Next to photoelastic analysis on model experiments [8, 9], split tools experiments have been used to spatially resolve the shear and normal stress distribution on the chip-tool interface [10, 11]. A typical result of split tool experiments is that shear stress grows linearly with the normal load (constant coefficient of friction, i.e. Amontons law) but is bounded by some constant [2].

The fact that the frictional stress grows linearly with the normal load and levels off to some constant value has been attributed to the surface roughness of the tool chip interface. In line with the Bowden and Tabor [7] picture, the macroscopic friction force is proportional to the real area of contact. The constant of proportionality is the theoretical shear stress required to separate the adhesive micro contacts formed between tool and chip. At the same time, the real area of contact grows with the normal load until it is large enough to support the load. If one assumes that plastic deformation dominates the growth of the real contact area, which is a reasonable assumption for metals, the plastic flow stress determines the growth rate with external load. Thus, the friction coefficient is a constant given by the ratio of theoretical shear stress and plastic flow stress. When the normal load is high, the real contact area approaches the apparent one, which explains the shear stress plateau in the vicinity of the cutting edge. In the high shear stress regime, the chip flows due to plastic deformation in the vicinity of the interface—the so-called secondary shear zone—but no relative motion occurs between the chip and the tool. This region is often referred to as the “sticking zone” and its extent is given by the cutting length l_c . Beyond l_c sticking changes into sliding and friction is determined by an Amontons–Coulomb type friction model with constant coefficient of friction μ .

Finnie and Shaw [12] suggested an empirical relation for the real area of contact A_r as a function of the normal load σ_n in the context of metal cutting

$$A_r = A_a(1 - \exp(-B\sigma_n)), \tag{1}$$

where A_a is the apparent area of contact and B is a constant parameter. Equation (1) can be translated into a similar expression for the frictional stress [13]

$$\tau_f = mk[1 - \exp(-B\sigma_n)], \tag{2}$$

where k is the plastic flow stress of the work material and m is a constant $0 < m \leq 1$. Note that B is usually approximated as $B \approx \mu/mk$, which can be easily found by linearizing Eq. (2) at small normal loads and extrapolating to the

plateau stress. A variation of this model has been introduced by Dirikolu et al. [14] with an additional empirical parameter a

$$\tau_f = mk[1 - \exp(-(\mu\sigma_n/mk)^a)]^{1/a}, \tag{3}$$

which allows fine-tuning the transition from sticking to sliding regime. Alternatively, instead of assuming a smooth transition from sticking to sliding, a piecewise formulation [15, 16]

$$\tau_f = \begin{cases} \mu\sigma_n, & \mu\sigma_n < mk, \\ mk, & \mu\sigma_n \geq mk, \end{cases} \tag{4}$$

is often used, and referred to as the *sticking-sliding* friction model. An overview of the most commonly used friction models is given in Fig. 1.

Although material parameters in these models can in principle be obtained from experiments, severe cutting conditions often do not allow direct experimental parametrization (with few exceptions, see e.g. [17–19]), and would require extrapolation to e.g. high strain rates. Therefore, results of the cutting process itself are often used to optimize model parameters, for instance by comparing measured cutting forces with simulated ones [20–22]. Özel et al. [16] investigated the influence of different friction models implemented in the FE code Deform2D based on a comparison of simulated cutting forces with experiments. They found the best agreement for variable friction across the rake face, where parametrization of the friction coefficient comes either from experiments or from an empirical relation by Dirikolu et al. [14] [Eq. (3)]. While most studies compare different friction models as implemented in a specific solver, Malakizadi et al. [23] compared the outcome of cutting simulations

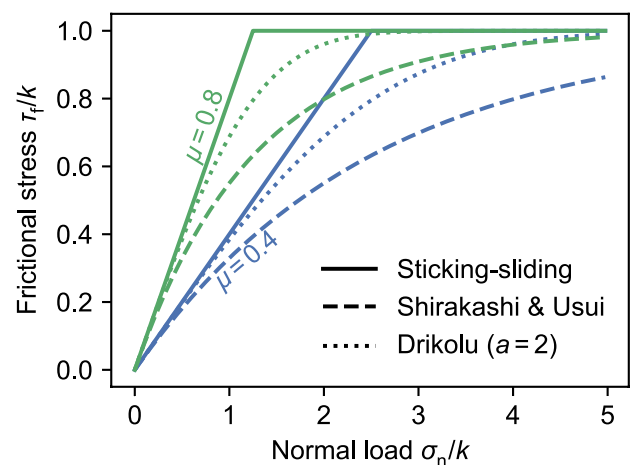


Fig. 1 Overview of commonly used friction models. The transition from the sliding regime at low normal load to the sticking regime with constant shear stress is either modelled as a piecewise linear function [Eq. (4)] or continuously [Eqs. (2), (3)]. All stresses are normalized by the flow stress k and $m = 1$

(chip thickness, contact length, cutting force, feed force) also across FE implementations. While sticking-sliding [Eq. (4)] and pressure-dependent models [Eq. (3)] performed best on average when compared to experiment, large relative errors of the individual output responses persisted. More surprisingly, implementations of the same friction model in different solvers led to diverse results.

Friction coefficients obtained by calibration to experiment can be seen as a fudge factor rather than a material parameter describing the physical processes at the interface. Therefore, predictive abilities of the cutting simulations are limited within the range of experimental calibration, which also limits the opportunities given by the numerical tools developed over the years. In this work, we attempt to calibrate a friction model based on experiments and numerical simulations of individual physical effects involved in friction, without using the full cutting process for calibration. Instead, the cutting experiment is only used to validate our approach. The real area of contact between the tool's rake face and the formed chip, as well as the theoretical shear stress between those surfaces, are the main ingredient of most of the friction models used today. Orthogonal cutting experiments with a microtextured tool allow us to align chip and tool topographies w.r.t. each other, leading to an *ex situ* reconstruction of the rough interface during cutting. Numerical contact mechanics simulations and hardness measurements then provide the relative contact area. Furthermore, we use density functional theory molecular dynamics (DFTMD) simulations to obtain the pressure-dependent theoretical shear stress of a hypothetical tribofilm formed at the interface of the considered material pairing. The atomic composition of the tribofilm is obtained from X-ray photoelectron spectroscopy (XPS). This methodology provides a physically motivated approximation of the tool chip friction in metal cutting, which is validated with 2D FE chip forming simulations and experiments.

2 Materials and Methods

2.1 Experimental Program

2.1.1 Cutting Conditions

The tests were carried out using samples of AISI4140 with dimensions of $\varnothing 120 \times 4$ mm, which were previously

quenched and tempered at 600° C for one hour in accordance with DIN EN ISO 18265. The resulting hardness is 339 ± 10 HV30, which gives a tensile strength of 1070 ± 31 MPa according to DIN EN ISO 18265. The material's chemical composition is given in Table 1.

The orthogonal turning tests were carried out using a 3-axis milling machine of type POSmill CE 1000 as shown in Fig. 2. The workpiece is clamped in the tool spindle and the cutting speed is set via diameter-dependent rotation speed. The different rake angles can be set by rotating the upper part of the toolholder, which is clamped to a Kistler Type 9255 dynamometer (Fig. 2a). The forces are recorded with a frequency of 10 kHz in direction of cutting force (F_c) and passive force (F_n) during the experiments.

To determine the forces in the process, a carbide cutting insert of type K30 according to ISO 513 with an Alcrona Pro coating from Oerlikon Balzers with a rake angle of $\gamma = 0^\circ$, a clearance angle of $\alpha = 3^\circ$ and a cutting edge rounding of $r_\beta = 20\mu\text{m}$ without chip breaker was used. To avoid the influence of wear, the cutting inserts were only used once per trial. To determine the contact length, microtextures were applied to the rake face at a defined distance and angle to the cutting edge using the procedure described in Ref. [24]. The applied micro textures with a depth of 10 μm and a width of 50 μm according to Fig. 2c are reproduced inversely on the underside of the chip during machining and enable the immediate determination of the real contact length l_c as well as the ascertain alignment of the two surfaces in contact.

The cutting velocities, uncut chip thicknesses, and rake angles were chosen to represent the challenging cutting conditions of gear skiving with an analogous orthogonal cutting setup. Therefore, parameter fields for the manufacturing of a ring gear in e-mobility applications [25] were exported using the freely available software *OpenSkiving* [26]. Given the parameter field, the maximum and minimum values were extracted and transferred into a central composite test design according to Table 2.

In order to investigate the influence of cooling lubricants on the described forces as well as on the contact length, and, thus, the influence of the tribological regime between the formed chip and the cutting tool, the tests were carried out with and without the presence of cooling lubricant. The mineral oil based "FUCHS ECOCut 715LE" was used as cutting fluid. For the oil-cooled experiments, the fluid pressure was set at 6 bar with a nozzle internal diameter of 4 mm. To ensure that the fluid is applied to the desired location, the cooling nozzle is pointed directly at the cavity formed

Table 1 Chemical composition of AISI4140 steel (wt%)

C	Mn	Si	P	S	Cr	Mo	Cu
0.41	0.81	0.33	0.01	0.023	1.04	0.189	0.13

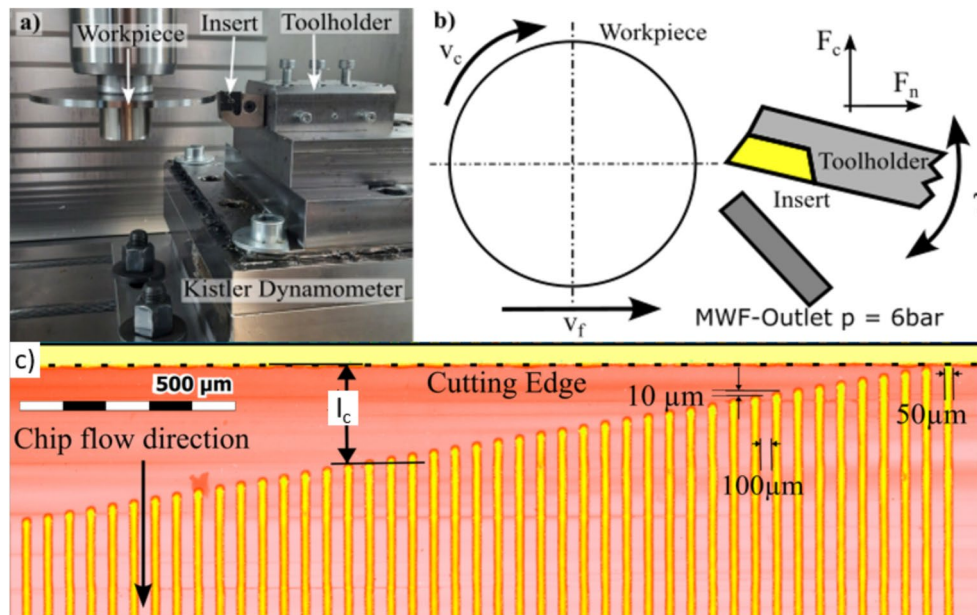


Fig. 2 a Test setup of orthogonal cutting tests. b Schematic drawing of experimental setup. c Microtextured rake face

between the chip and the tool (Fig. 2b). In addition, the variation of the cooling strategy for the force measurement and the determination of the contact lengths were each repeated three times to ensure statistical validation.

2.1.2 Post Experimental Measurements

In order to determine the surface topography, the tools and resulting chips were analyzed using a confocal microscope of the type Nanofocus μ Surf Custom. In this case, an objective with a magnitude of 20 for the chip surface and an objective with a magnitude of 50 for the cutting tool, a numerical aperture of 0.4, and a resolution in the height direction of 6 nm was used.

In addition, the hardness of the chips formed was measured after the tests. For this purpose, the hardness changes of the chips under different thermomechanical loads were measured in a first step, where the samples with the expected lowest (mild) and greatest (severe) thermomechanical load were selected according to Table 2. For the hardness measurement, the chips were embedded in two component resin, ground, and polished to mid-height. The hardness was subsequently measured, with a Qness Q10 hardness tester and a test load of 100 g, which corresponds to HV0.1. For a representative average hardness value, several test indentations were made, which were distributed randomly over the chip surface.

XP spectra of the cutting tool were obtained with monochromatic Al $K\alpha$ (1486.7 eV) X-rays using a ULVAC PHI 5000 VersaProbeTM II (Physical Electronics Inc). The spot

size of the measurements was 200 μm . Elemental depth profiles were measured with the same spot size, utilizing argon ion sputtering with either 1 keV or 2 keV acceleration voltage and 50 mA current. The depth scale was calibrated using a SiO_2 wafer with a predetermined surface thickness. Quantification of the elemental composition was performed

Table 2 Overview of considered cutting parameters

Trial-nos	Rake angle	Uncut chip thickness	Cutting speed v_c (m/min)
	γ ($^\circ$)	h_c (μm)	
1 (mild)	-5	50	115
2	-5	50	140
3	-5	150	115
4	-5	150	140
5	-5	100	127.5
6	-15	100	115
7	-15	100	140
8	-15	50	127.5
9	-15	150	127.5
10	-15	100	127.5
11	-25	50	115
12	-25	50	140
13	-25	150	115
14 (severe)	-25	150	140
15	-25	100	127.5

All cutting conditions have been investigated under dry and lubricated conditions. Bold lines correspond to the two cases used for calibration of the friction model

using the MultiPAKTM software package from Physical Instruments.

2.2 Contact Mechanics

We used the topography scans of the textured tools and the produced chips for contact mechanics calculations. The grooves of the textured tools have been used to estimate the dry contact length, as described in Ref. [24]. Here, the presence of the grooves on both tool and chip surface was further used to orient chip and tool w.r.t each other. The alignment of chip and tool topography scans allows retracing of the chip's sliding path over the tool, particularly in the untextured region, thereby providing insights into the frictional dissipation mechanisms. We performed elastic and elastoplastic contact mechanics simulations (no sliding) to determine the real area of contact for various normal loads, which we then used in our friction model.

2.2.1 Topography Pre-processing

Here, we briefly describe the workflow to get from the raw topography data of chip and tool surface scans to the composite roughness profiles used in the contact mechanics calculations. We denote the area scan of the tool with $h_t(\mathbf{r})$ and that of the chip with $h_c(\mathbf{r}')$. With the help of the grooves we rotate and shift the chip coordinate system into the tool frame $\mathbf{r} = \underline{R}(\mathbf{c}', \varphi)\mathbf{r}' - \mathbf{b}$, where \underline{R} is a two-dimensional rotation matrix around the center point \mathbf{c}' in the chip frame, φ is the angle of rotation, and \mathbf{b} denotes the shift vector. We used SciPy's [27] `ndimage.rotate` function to apply the coordinate transformation which uses bicubic spline interpolation internally, and the parameters φ and \mathbf{b} have been adjusted by visual inspection of the overlapping grooves (see inset of Fig. 3a). We selected a quadratic region with side length $s_x = 0.33$ mm in the untextured region of the tool and the corresponding region (now in the same coordinate system) of the chip (black squares in Fig. 3a and b). By adjusting the y -component of \mathbf{b} , we selected three chip tool replica pairs.

Before combining the selected chip and tool pairs to single composite topographies, we removed extreme outliers ($|h - \bar{h}| > 8\sigma$) from the topography that may stem from measurement artifacts. Furthermore, since chip and tool surfaces have been recorded with different resolutions, we adjust the chip resolution by filling the amplitude spectrum $\tilde{h}(|\mathbf{q}|)$ with zeros for all the "missing" frequencies in Fourier space, where $\mathbf{q} = (2\pi n/s_x, 2\pi m/s_y)$, and $n \in [1, N_x]$ and $m \in [1, N_y]$ denote the number of pixels in x and y -direction, respectively. For all cases considered here, we have $N_x = N_y = 1024$.

Following the adjustment of the chip resolution, we sandwiched the topographies $h(\mathbf{r}) = h_t(\mathbf{r}) + h_c(\mathbf{r})$ to obtain a composite rough surface which can be used in numerical contact mechanics calculations. At this point the composite surface still contained undefined data, which has been filled with interpolated data from a harmonic function by solving the Laplace equation at the undefined grid points with the surrounding pixels acting as Dirichlet boundary condition. Detrending by subtracting polynomial contributions up to second order complements the data pre-processing pipeline. We used *contact.engineering*'s Python API *SurfaceTopography* [28] for all topography pre-processing steps.

2.2.2 Elastoplastic Contact Calculations

We performed contact mechanics calculations using *contact.engineering*'s ContactMechanics Python API [28]. We considered both purely elastic and ideal elastic plastic material models as limiting cases for the determination of the real area of contact. In these calculations, we considered the composite rough topography as a rigid indenter which was pressed against a flat elastic (or elastoplastic) substrate (see Fig. 4b) with effective contact modulus E^* , where $1/E^* = (1 - \nu_1^2)/E_1 + (1 - \nu_2^2)/E_2$, where E_α and ν_α are the Young's moduli and Poisson's ratios of the contacting bodies, respectively. We used elastic parameters for steel ($E = 210$ GPa, $\nu = 0.3$) and AlCrN coatings ($E = 380$ GPa, $\nu = 0.2$) from the literature [29, 30]. For the plastic calculations, the indentation hardness p_Y of the softer material (i.e. the chip) was taken from the hardness measurements described above. Our contact mechanics calculations were performed under force control, where the displacement field is given by a convolution of the elastic surface Green's function with the pressure field, which can be efficiently solved in Fourier space using the fast Fourier transform (FFT) [31]. Our nonperiodic surface topographies were handled within the same FFT-based framework using a windowing scheme as described in Ref. [28]. The linear complementarity problem of contact mechanics, i.e. finding the contact area while enforcing nonnegativity constraints for pressure and gap distribution, was solved with a constrained conjugate gradient (CG) solver as described in Ref. [32] and implemented in *contact.engineering* [28]. In the elastic-ideal plastic case, the pressure is also constrained from above by p_Y as introduced in Ref. [33]. We refer to this approach as the saturation hardness model, which is equivalent to an elastic ideal plastic material behavior. Isotropic hardening has been previously introduced into the saturation hardness model [34], and even FFT-based solvers including von Mises plasticity exist [35, 36]. However, Frérot et al. [37] showed that the saturation hardness model gives acceptable results for global properties, such as the real contact area, which is our main quantity of interest. Furthermore, using the saturation hardness

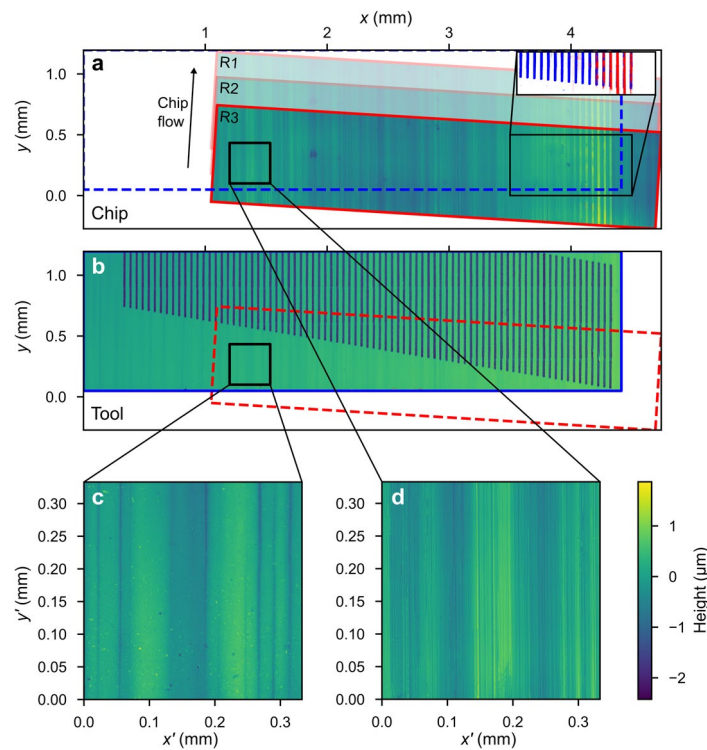
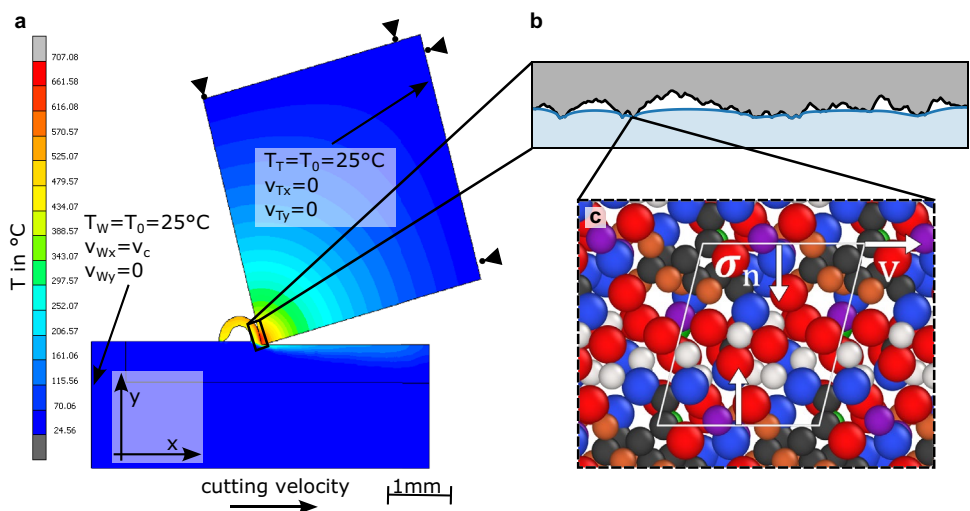


Fig. 3 Orientation of chip and tool topographies and selection of characteristic contact patches. **a** Chip topography after rotation into the tool coordinate system. The orientation angle and shift in x -direction has been chosen manually such that hills on the chip surface and valleys on the tool surface overlap (see inset in the top right corner). Since the chip moved in y -direction relative to the tool during cutting, overlapping chip tool replica pairs have been selected by shifting the chip topography in y (R1–R3). The amount of the shift has

been increased here for a better visual representation. **b** Tool topography with microtextured surface. We selected a small square with side length $s_x = 0.33$ mm in the untextured region of the tool surface (black square) for our contact mechanics simulations. The outline of the chip topography is shown as a red dashed line. **c** Magnified tool topography in the selected contact area. **d** Magnified chip topography in the selected contact area

Fig. 4 Overview of simulation methods. **a** Simulation setup for the 2D FE simulations. **b** Schematics of contact mechanics simulations with a rigid rough indenter (gray) and an elasto(plastic) halfspace (blue). **c** Setup of the molecular dynamics simulations of the sheared tribofilm. Color code: Al (silver), C (black), Fe (brown), Cr (purple), Mn (green), N (blue), O (red) (Color figure online)



model, our contact area predictions are less dependent on the resolution of the surface topographies, compared to an elastic calculation.

2.3 Atomistic Simulations

To determine the shear stress at the dry interface between chip and cutting tool, we performed DFT molecular

dynamics (DFTMD) simulations. Due to the harsh conditions in the dry contact between the hard ceramic surface of the cutting tool and metallic chip, severe cold welding is assumed. This is consistent with the XPS measurements of the composition of the cutting tool surface which indicate the simultaneous presence of elements from the machined steel, from the cutting tool itself, as well as oxygen. From the XPS measurements we deduced the following composition of the interfacial tribofilm: 16% Al, 16% C, 5% Cr, 12% Fe, 3% Mn, 16% N and 31% O and traces of Na and Ca. The stoichiometry of the modelled tribofilm material was chosen according to the experimental XPS results (see Fig. 8a). In total, ten pseudo-amorphous sample structures with composition $\text{Al}_{10}\text{C}_{10}\text{Cr}_3\text{Fe}_7\text{Mn}_2\text{N}_{10}\text{O}_{18}$ were generated and simulated to obtain a reasonable sampling of different initial structures.

Tribological boundary conditions representing shearing of the tribofilm (see Fig. 4c) were imposed by using Lees-Edwards boundary conditions. Normal loads of 0, 1, 2.5 and 4 GPa were applied by a Berendsen barostat along the direction normal to the shear plane. The temperature was controlled by a Langevin barostat to achieve a mean temperature of 1000 K. The Langevin barostat was acting only along the direction perpendicular to both the normal and sliding directions. The time constants of the Berendsen and Langevin barostats were set to 100 and 200 fs, respectively. Integration of the molecular dynamics was performed with a time discretization of 0.5 fs using the *Atomic Simulation Environment (ASE)* Python library [38]. Each of the DFTMD simulations for the different normal loads and amorphous samples were performed for at least 10^5 time steps corresponding to at least 50 ps simulation time. The resulting shear stresses were determined by averaging over the second halves of the simulation runs to exclude the equilibration phase.

Forces, energies, and stresses were calculated on the DFT level by using the CP2K code [39] and by employing the PBE functional [40]. Kohn-Sham orbitals were expanded in the DZVP-MOLOPT-SR-GTH basis set [41] and GTH pseudopotentials [42] were employed. The plane wave cutoff determining the resolution of the finest integration grid on which the Gaussian basis functions are represented was set to 8.16 keV.

2.4 FE Chip Forming Simulations

2D FE-simulations were performed for 15 different experimental study points using MSC Marc 2023 [43]. The simulations were performed using the implicit time integration with the dynamic transient operator Single-Step Houbolt, for the dynamic time step analysis. A multifrontal direct sparse solver with the full Newton-Raphson iterative procedure was selected. The selection of the time step size is based on the minimum element edge length and the cutting speed to ensure a stable simulation of the cutting process.

The model consist of a rigid tool with a variable Tri-Mesh and heat sinks, which indicate the thermal boundary conditions of the workpiece and tool. Further, the workpiece is set up with quadrilateral elements under plane strain assumption and continuous re-meshing depending on refinement boxes, element distortion, and strain change, resulting in a minimum element edge length of $6\ \mu\text{m}$ [44–46] (Fig. 4a). For the contact formulation, a node-segment approach is used in which the contact between deformable bodies with a rigid body is treated via a one-point constraint equation (SPC). A sticking-sliding friction model similar to Eq. (4) is used, whose parametrization with experiments and multiscale simulations is detailed below.

For modeling the workpiece material, the Johnson-Cook plasticity model [1] commonly applied in machining simulations is used,

$$\sigma_f = [A + B\bar{\epsilon}^n] \left[1 + C \ln \left(\frac{\dot{\epsilon}}{\dot{\epsilon}_0} \right) \right] \left[1 - \left(\frac{\theta - \theta_{\text{room}}}{\theta_m - \theta_{\text{room}}} \right)^m \right], \quad (5)$$

where σ_f denotes the temperature and strain rate dependent plastic flow stress. The model parameters are given in Table 3 according to previous work [47], where A is the yield strength, B is the hardening modulus, C is the strain rate sensitivity coefficient, n is the hardening coefficient, and m is the thermal softening coefficient.

In addition, the temperature-dependent material properties were implemented in the model according to Refs. [48–50]. The cutting edge rounding was set to $20\ \mu\text{m}$, measured optically with a Keyence VHX-7000 by surveying the real geometry. Further parameters, which were kept constant during the simulation, are listed in Table 4, while the heat transfer coefficients to the environment were varied depending on the cooling method according to Ref. [51].

3 Results

3.1 Hardness

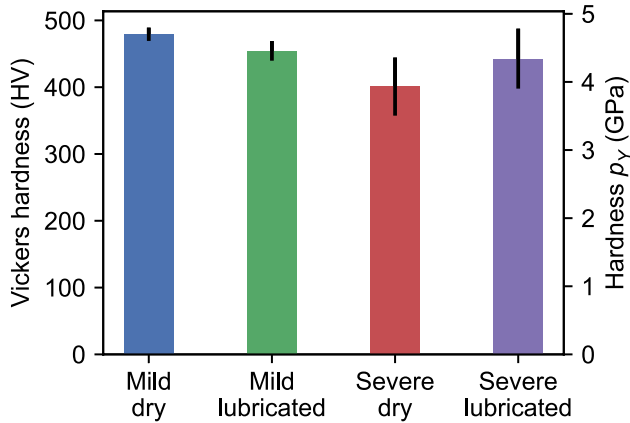
Figure 5 shows the results for the Vickers indentation hardness tests for the four considered cutting conditions. We report the results both in Vickers hardness (HV) and converted into an equivalent hardness value in units of stress. The average hardness under mild conditions is slightly higher than that of the chips produced at the most severe cutting conditions. Furthermore, for the mild conditions, the application of cooling liquid slightly decreased the average indentation hardness. The opposite is true for the severe conditions, where lubrication leads to harder chips. For the mild conditions, ten indentations have been performed on a single chip, and under severe conditions, 30 and 20 indentation samples have been recorded for dry and lubricated

Table 3 Johnson-Cook parameter

A (MPa)	B (MPa)	C (-)	n (-)	m (-)
595	580	0.023	1.03	0.133

Table 4 Constant parameters used in the FE simulations

θ_m (K)	θ_{room} (K)	λ_c (W/mK)	$\dot{\epsilon}_0$ (-)	α_{air} (W/m ² K)	α_{oil} (W/m ² K)
1820	298	120	1	23	2500

**Fig. 5** Result of the hardness measurements. Mean and standard deviation of ten indentations for the mild conditions, and 30 (20) indentations for the dry (lubricated) severe conditions

processing, respectively. We show the standard error of the mean as an error bar in Fig. 5. Severe cutting conditions led to a higher variance in the indentation hardness compared to the mild cutting conditions. Except for the higher variance under severe cutting conditions, our data does not show a significant influence of the cutting conditions on the chip hardness. The experimental hardness measurements (in SI units) will be used as a material parameter in the elastoplastic contact mechanics calculations with saturation hardness.

3.2 Roughness

Figure 6 shows the topographies of chip, tool, and the composite surfaces for a single replica and four different cutting conditions. The first two rows of Fig. 6 correspond to the mild cutting conditions under dry and lubricated conditions. The third and fourth row correspond to severe dry and lubricated cutting conditions, respectively. On both of the individual topography scans (first two columns) distinct features such as grooves in the cutting direction can be seen. Peaks on the chip surface seem to correspond to valleys on the tool surface. This becomes more obvious for the composite surfaces (third column), where most of these features vanish.

The similarity between chip and tool surfaces is further illustrated as line scans perpendicular to the cutting direction, as indicated by the orange and blue lines in the 2D scans. These one-dimensional profiles are illustrated in the fourth column, where the chip surface is stacked upside-down on the tool surface, representing the chip tool contact during the experiments. Note that the line profiles in the fourth column are shifted to visualize their conformity.

While the good match between chip and tool topography is already visible with the naked eye, we then turned to a more quantitative description of the surfaces. Figure 7 shows the root-mean-square (RMS) roughness for the four cutting conditions. Presented roughness values correspond to an average over three replicas for each chip tool pair, but differences among the replicas are generally small (replicas are not entirely independent since there is overlap). The average RMS roughness of the chip surface is larger than that of the tool surfaces in all considered cases. The composite surface created through a combination of chip and tool surface have lower roughness in the case of mild cutting conditions. For the severe cutting conditions, the roughness of the composite surface is similar to that of the chip.

3.3 Interfacial Shear Stress of the Tribofilm

Figure 8a shows an XPS depth profile recorded on one of our cutting tools. The concentration of the main constituents of the Alcrona Pro cutting tools (Al, Cr, and N) saturate at a depth of around 150 nm. Oxygen and carbon can be found in high concentration ($\sim 35\%$ and $\sim 60\%$, respectively) in regions close to the surface, and their concentrations gradually decay towards the bulk. Furthermore, in the first 100 nm below the surface, oxidized iron is present at a concentration of around 10%, which gradually changes into metallic below 100 nm (where oxygen is less abundant). Low Mn content ($< 5\%$) can be found, as well as traces of Na and Ca. The dashed vertical line in Fig. 8a highlights the composition tested with DFTMD, which we assume to be representative for a tribofilm formed at the tool chip interface.

Shear stresses as a function of the applied normal load of the hypothesized amorphous tribofilm material calculated by DFTMD simulations are shown in Fig. 8b. There is some scattering of the normal load and shear stress values due to the finite simulation times. However, there is a clear, yet relatively weak dependence of the shear stress on the normal load. Due to the scattering in both normal load and shear stress, we performed orthogonal distance regression (ODR), and found a good fit for a quadratic relation between shear stress and normal load,

$$k(\sigma_n) = \tau_0 + a\sigma_n + b\sigma_n^2, \quad (6)$$

with fit parameters in Table 5.

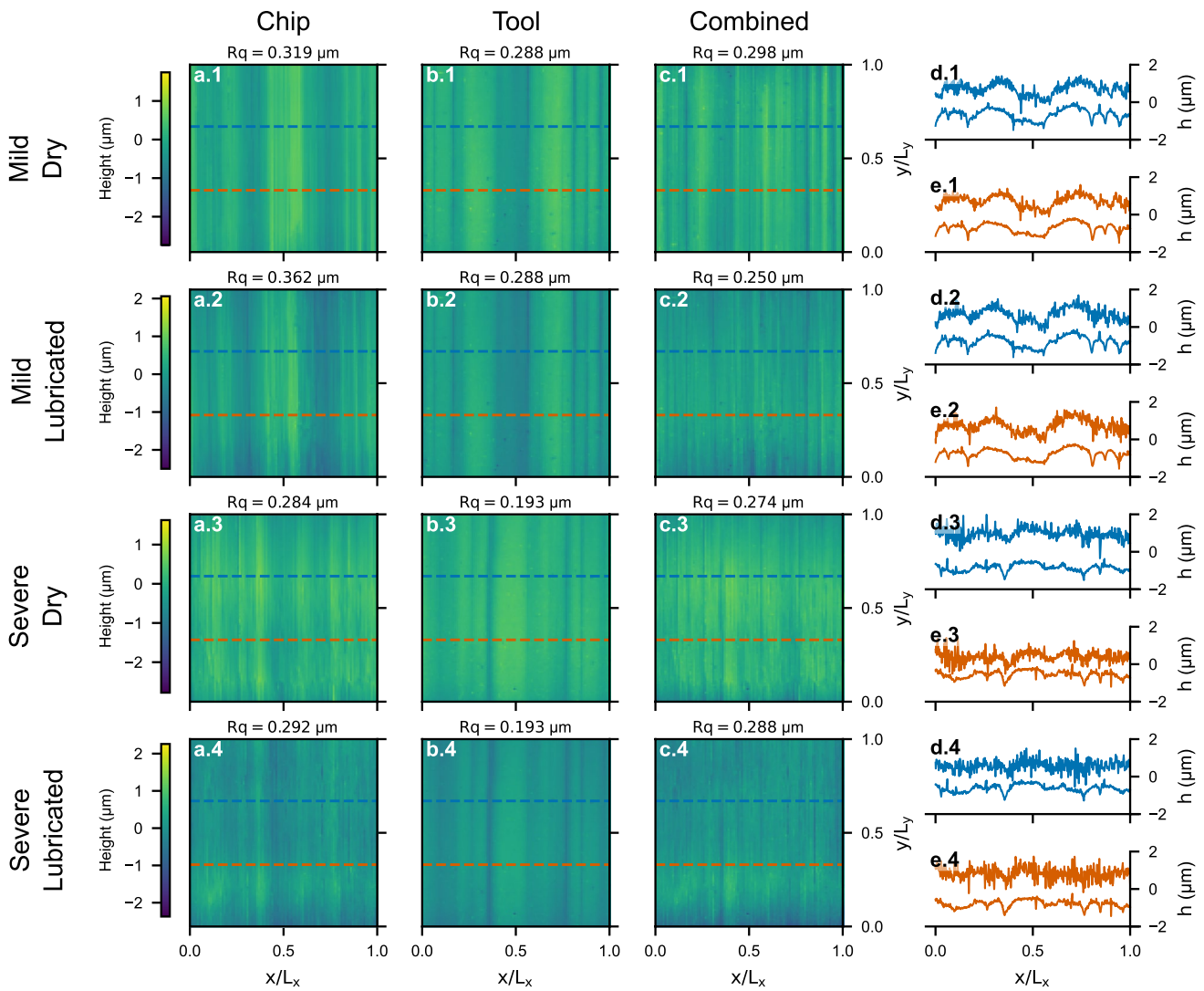


Fig. 6 Overview of topography scans for a single replica under different experimental conditions. Column **a** shows the post-processed topography scans for the chip, column **b** for the tool, and column **c** for the combined (i.e. sandwiched) topography as used in the contact mechanics calculations. **d** and **e** are line scans perpendicular to the cutting direction at the locations indicated by dashed horizontal lines in columns **a–c**. Chip (upper) and tool (lower) line profiles have been slightly shifted to positive and negative mean heights, respectively, in

order to highlight their high level of conformity. Rows correspond to different experimental conditions, as shown in Table 2. The indicated root-mean-square (RMS) roughness values R_q are averages over all available line scans in the direction perpendicular to the cutting direction. Note that the same tool has been used for mild and severe cutting conditions, therefore panels **b.1** and **b.2** as well as **b.3** and **b.4** are the same but appear to be different due to different color scales

3.4 Real Contact Area and Friction Model

Figure 9 shows the real area of contact as a function of the normal load as a result of the contact mechanics calculation. In Fig. 9a, we compare a purely elastic material model with an ideal elastic plastic behavior as implemented by the saturation hardness model in our contact mechanics simulations. Assuming elastic behavior, much higher normal loads are required to reach fractional contact areas of only a few percent when compared to the ideal plastic case. The ideal plastic contact approaches full contact at the saturation pressure

(as given by the hardness measurements) linearly, while the elastic curves show the typical S-shape requiring infinitely large loads in the full contact limit (note the logarithmic load axis in Fig. 9a). The dashed line in Fig. 9a represents a fit to the Finnie and Shaw model, Eq. (1), which gives an excellent fit to the numerical simulations. Figure 9b shows the relative contact area for the plastic contact simulations for the four considered cutting conditions on a linear load axis. The linear increase of the contact area with applied load for the ideal plastic case becomes more obvious here. The simulations were run until 80% fractional contact was

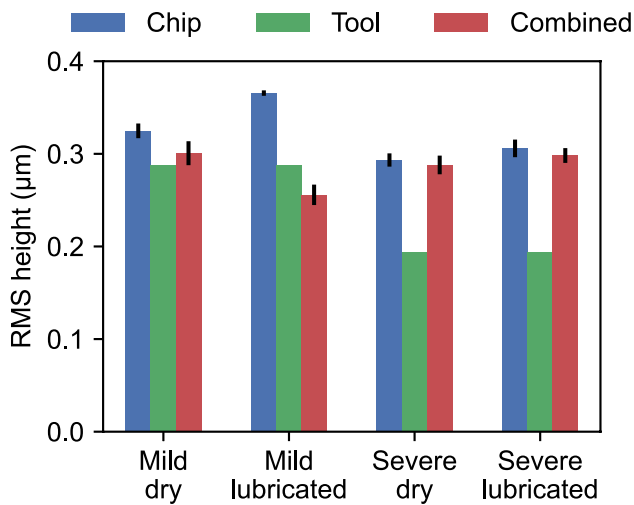


Fig. 7 Overview of measured scalar roughness parameters for all selected samples. The root-mean square roughness was measured orthogonal to the cutting direction for the individual patches selected from chip and tool surfaces, and the resulting roughness of the composite samples. Errorbars correspond to the standard deviation of the three replicas

reached. When extrapolated to 100% relative contact area, the limiting load coincides with the experimentally measured hardness, while roughness does not seem to play a significant role for the contact area (see also Fig. S1).

The resulting frictional stress $\tau_f = k(\sigma_n)A_r/\sigma_n A_a$ is based on the numerical calculations of contact area A_r and shear stress k as a function of the normal load σ_n , and is shown in Fig. 10a for the four considered cutting conditions. In the sliding regime, the Coulomb type friction model leads to an approximately linear increase of frictional stress with the applied normal load. Slight deviations from the linear behavior come from the pressure-dependent shear stress obtained from the DFT calculations. This can be seen in

Fig. 10b, where the friction coefficient, i.e., the slope in the sliding regime, is plotted against the normal load. We obtained friction coefficients between 0.5 and 0.7 depending on the cutting conditions and the normal load. Shifts among the four considered cutting conditions in the friction coefficients directly correspond to the differences in the hardness measurements (cf. Figure 5) while the pressure dependency originates in the theoretical shear stress (cf. Figure 8b) which is the same for all four cases.

Since roughness seems to play a minor role when considering ideal elastic plastic surface deformation, the contact area can simply be approximated with a linear function $A_r = A_a \sigma_n / \sigma_Y$, which is one of the key assumption in the Bowden and Tabor model [7, 52]. Thus, the frictional stress becomes

$$\tau_f(\sigma_n) = \begin{cases} \mu(\sigma_n)\sigma_n, & \sigma_n < p_Y, \\ k(\sigma_n), & \sigma_n \geq p_Y, \end{cases} \quad (7)$$

with $\mu(\sigma_n) = k(\sigma_n)/p_Y$ and $k(\sigma_n) = \tau_0 + a\sigma_n + b\sigma_n^2$. Parametrization of $k(\sigma_n)$ stems from the DFTMD simulations (with ODR fit parameters a , b , and τ_0 from Table 5) and p_Y from hardness measurements.

3.5 FE Chip Forming Simulations

The described friction model was implemented into the FE chip forming simulations following Eq. (7). Figure 11 shows the measured forces and contact lengths in comparison to the corresponding simulation results for the investigated experimental parameters according to Table 2. The simulation results for the different cooling methods are presented as one result, as the change of the heat transfer coefficient had no influence on the parameters to be evaluated. The test results of the air cooling are shown in blue, the tests with oil cooling are shown in green, and the results of the

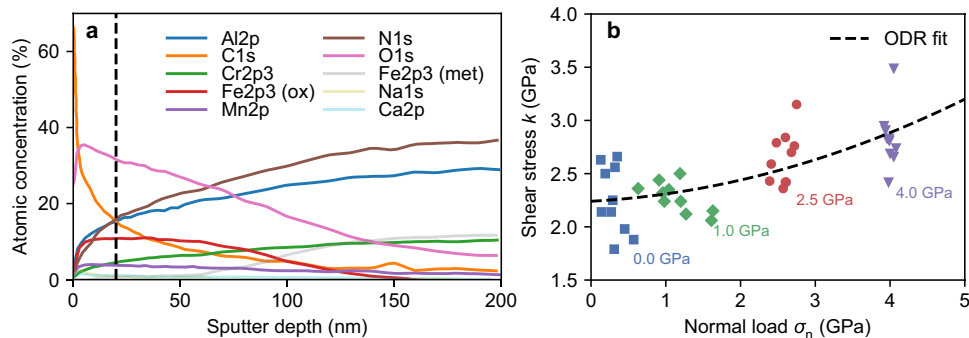


Fig. 8 Composition and shear stress of the tribofilm. **a** Atomic composition along the depth of the cutting tool. The dashed vertical line corresponds to the composition tested with density functional theory (DFT). **b** Theoretical shear stress as a function of the normal pressure

from DFT calculations. The dashed line describes the result of a fit to a quadratic polynomial using orthogonal distance regression (ODR). Numbers in the plot refer to the corresponding target normal load in the simulations

simulation, and, thus, the validation of the derived tribological model in the 2D chip formation, are shown in red. The cutting forces are shown in comparison in Fig. 11a. It is evident that there is no recognizable influence of the cooling lubricant on the resulting forces. Furthermore, the simulated results show good agreement with the experimental values. However, it was found that the force in the simulation tends to be underestimated for smaller negative rake angles and overestimated for large negative rake angles. This effect is also evident in the passive forces shown in Fig. 11b. Overall, according to Table 6, the prediction accuracy of the simulation can be specified at an average error of 5% with a

maximum deviation of 11% for the cutting forces and 11% for the passive force with a maximum deviation of 30%. Cutting velocity seems to have a minor effect on the prediction of forces, but the contact length prediction is highly velocity dependent (e.g. compare test 1 and 2, or 3 and 4). Furthermore, no decisive influence of the use of oil on the contact length can be determined for the contact lengths shown in Fig. 11c. During the determination of the contact length, as described in Sect. 2, clear imprints of the microtexturing could be detected in the chip surface (“w/o blur”), which correspond to the depth of the texturing of the cutting inserts (10 μm). In contrast, the measured values indicated with “w/ blur” also represent imprints between 5 μm and 10 μm, and therefore lie below the ultimate strength of the material and must therefore still be counted as part of the contact length. Similar to the comparison of the experimental forces with the simulation results, the contact lengths show satisfactory agreement. An average prediction error of 5.5 % can be determined. The maximum deviation from experiment to simulation was found to be 16%

Table 5 Fit parameters from orthogonal distance regression to the pressure-dependent shear stress data generated in density functional molecular dynamics (DFTMD) simulations

a (-)	b (GPa ⁻¹)	τ_0 (GPa)
0.038	0.031	2.240

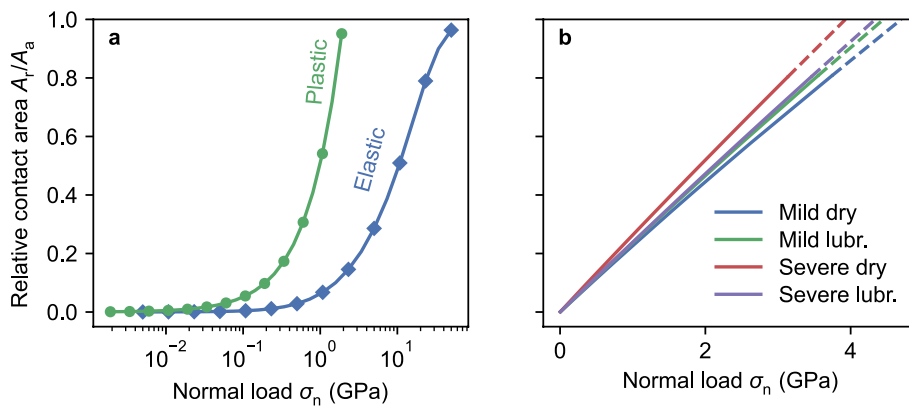


Fig. 9 Real area of contact for elastic and plastic contact. **a** Comparison between elastic and perfectly plastic contact area calculations for a single replica of the mildly loaded and lubricated sample. Across all samples, there is no significant influence of the interface roughness on the contact area. **b** Result of the contact area calculations

with ideal plastic deformation for all cutting conditions (replica 1). The contact area grows linearly with the applied load (note that the load axis is linear and not logarithmic as in **a**). Simulation results are shown until 80 % contact area (solid lines) and then extrapolated to the experimentally obtained hardness (dashed lines)

Fig. 10 Frictional stress and coefficient of friction from experimental and simulated data. **a** The frictional stress grows approximately linear with the normal load. **b** The friction coefficient as a function of the normal load. Differences are due to the hardness and pressure sensitivity from the theoretical shear stress calculated with DFT

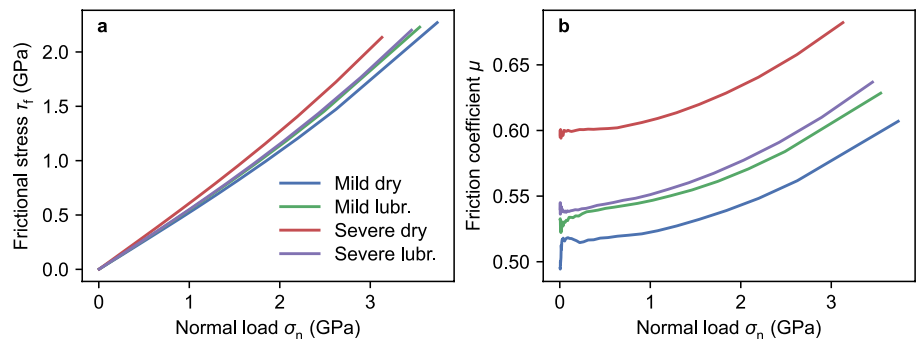


Fig. 11 Comparison of experimental results with finite element simulations for cutting forces (a), passive forces (b) and contact lengths (c)

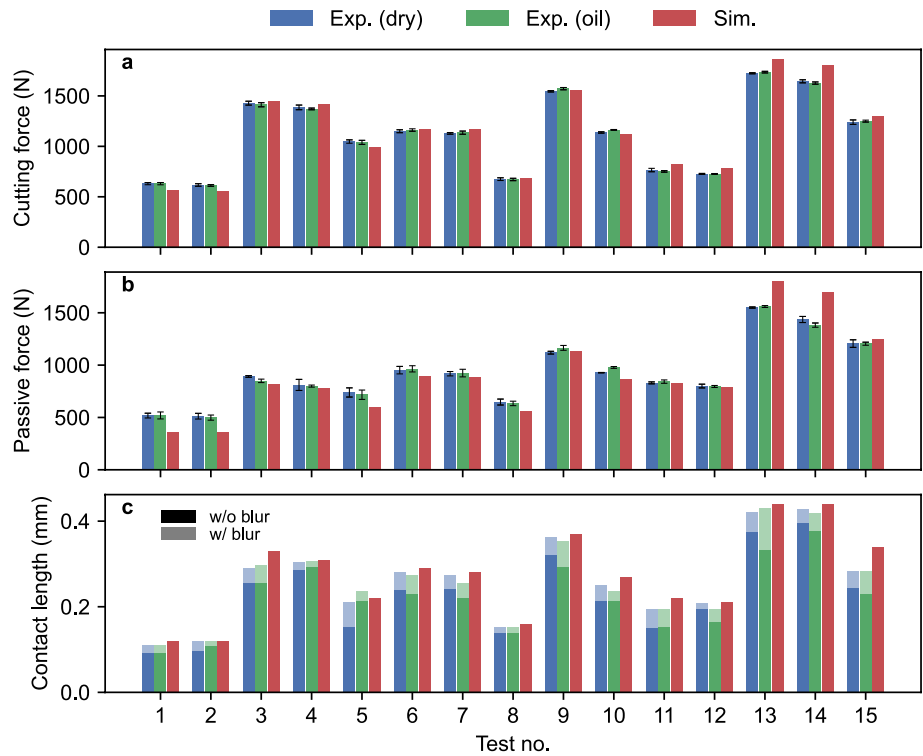


Table 6 Comparison of experimental data and simulation in terms of the relative error w.r.t. the experimental results

Test no.	γ ($^{\circ}$)	h_c (μm)	v_c (m/min)	$\Delta F_{c,dry}$ (%)	$\Delta F_{c,oil}$ (%)	$\Delta F_{p,dry}$ (%)	$\Delta F_{p,oil}$ (%)	$\Delta l_{c,dry}$ (%)	$\Delta l_{c,oil}$ (%)
1	-5	50	115	-10	-10	-30	-30	9	9
2	-5	50	140	-10	-9	-30	-28	0	0
3	-5	150	115	1	3	-8	-4	13	11
4	-5	150	140	2	3	-4	-3	2	1
5	-5	100	127.5	-6	-5	-19	-17	5	-7
6	-15	100	115	2	1	-6	-7	4	5
7	-15	100	140	4	3	-4	-4	3	10
8	-15	50	127.5	2	2	-14	-12	6	6
9	-15	150	127.5	1	-1	2	-2	2	5
10	-15	100	127.5	-1	-3	-7	-12	8	14
11	-25	50	115	7	9	-1	-2	13	13
12	-25	50	140	8	8	-1	-1	1	8
13	-25	150	115	8	8	16	15	5	2
14	-25	150	140	10	11	18	23	3	5
15	-25	100	127.5	4	3	4	4	20	20
Average deviation				5	5	11	11	6	8

4 Discussion

Cutting with micro textured tools is a common technique, e.g. to improve wear resistance [53, 54] in dry machining or to enhance lubrication [55, 56]. Recently, some of us have suggested the use of micro textured tools to measure the contact length in orthogonal cutting [24]. In this work, we

leverage the presence of the grooves and their imprint on the chip to align surface topographies of the tool and the formed chip with respect to each other (see Fig. 3). The line connecting the end points of the grooves forms an angle with the cutting edge, originally intended to estimate the contact length. This enabled us to investigate the tool chip contact region close to the cutting edge, which is unaffected by the grooves. The measured chip surface topography is an almost

perfect negative of the tool surface, which can be seen with the naked eye for various cutting conditions in Fig. 6. Thus, for the considered processing conditions, the metal working fluid seems to have no lubricating effect (in the sense of a separation of tool and chip surface) in the considered region close to the cutting edge. This is in line with results from previous work of us, where orthogonal cutting was investigated with a combination of fluid and solid mechanics simulations [46].

The roughness of the combined surface topographies is slightly reduced under mild cutting conditions, and the reduction is stronger when lubricant is used as shown in Fig. 7. However, it seems like mostly long wavelength contributions to roughness cancel in the combined topographies, particularly under mild conditions, while short wavelength roughness persists. Therefore, comparing scalar roughness parameters is not the right metric to judge the degree of conformation between tool and chip, which does not capture the multiscale nature of roughness [57].

Our friction model relies on two main assumptions: (1) the real area of contact is dominated by the hardness of the workpiece material, and (2), the newly generated steel surface adheres to the ceramic tool surface at the points of contact, forming an amorphous tribolayer at the interface. The first hypothesis is well-supported by the fact that the cutting tool is much harder than the work material, particularly at elevated temperatures, but the question arises what hardness means in that context, and how it may enter the model.

Hardness, as measured in an indentation experiment, depends on both elastic and plastic behavior of the material, but it is not advisable to infer related properties from a single hardness test. Furthermore, the severe microstructural modifications induced by the cutting process modify the plastic response of the work material. Here, we chose a pragmatic approach to include experimentally obtained hardness values (Fig. 5) of the produced chip surfaces directly into a numerical calculation of the contact area. As shown in analytical [58, 59] and previous numerical works [33, 34, 37], for materials with low hardness to stiffness ratio (such as metals), the contact area grows linearly with normal load up to full contact. Our elastic–plastic contact mechanics calculations based on measured topographies and hardness are no exception, and thus, the model parametrization could be done without extensive numerical calculations of the contact area.

The XPS depth profile in Fig. 8a shows that next to the constituents of the ceramic tool coating, Al, Cr, and N, carbon, iron oxide as well as alloying elements of AISI4140 can be found in a thin surface layer (< 100 nm) of the tool, which supports our second hypothesis. The high carbon content is particularly interesting, since carbon-based surface coatings are well-known to reduce wear and provide extremely low

friction [60, 61]. Recently, the *in-situ* formation of diamond-like carbon (DLC) from ambient hydrocarbons has been observed on Pt-Au alloys [62]. Such tribochemical effects are also of growing interest for metal cutting [63–66], where machining under dry conditions may replace wet machining processes, due to environmental constraints on the use of metal working fluids.

Above, we concluded that the lubricating effect in the vicinity of the cutting edge is negligible, effectively leading to dry contact, which would contradict the formation of a carbon-rich surface film from the lubricant. However, carbon may still be present at the interface due to hydrocarbon diffusion and contamination, or may come directly from the virgin steel surface. Furthermore, iron was transferred to the cutting tool surface and reacted with ambient oxygen, possibly enhanced by the harsh cutting conditions (i.e. tribo-oxidation). Since we cannot infer with certainty the origin and role of the high carbon content in the surface layer, we selected an atomic concentration at a depth of 20 nm, where the carbon content is reduced to about 16% and the iron oxide content has saturated, to be representative for the tribofilm. The pressure-dependent shear stress (see Fig. 8b) calculated with DFT-based MD is based on that concentration, which enters the friction model in both the sticking and sliding regimes. A detailed analysis of the variation of tribofilm composition with cutting conditions, and its influence on the interfacial shear stress is out of the scope of this work, but might be the subject of future work.

Hardness measurements have been performed at room temperature. However, temperatures during cutting can rise substantially up to 75% of the melting point depending on the cutting conditions, as evident from our FE simulations and known from experiments [67–69]. We found that the hardness of the work material mostly determines the friction coefficient in our model, particularly in the sliding regime, but we have so far not considered thermal softening. In contrast, the shear stress of the tribofilm has been recorded at elevated temperatures (1000 K) with our DFTMD simulations, and we have not sampled along the temperature axis to calibrate its sensitivity due to temperature changes. Hence, we assume that the temperature-dependence of the shear stress of the amorphous tribofilm is negligible at high normal loads, and likewise consider a constant, temperature-corrected hardness in the following. Thermal softening in metals and alloys is related to dislocation climb, which is why Arrhenius-type relations have been suggested to describe the hardness reduction [70]. Torres et al. [71] extensively tested the temperature dependent hardness for various steel grades at elevated temperatures and suggested using up to three distinct slopes (activation energies) to describe the hardness over a wide range of temperatures. For simplicity, we assume a single empirical relation $H_{RT}[1 - A \exp(-B/T)]$,

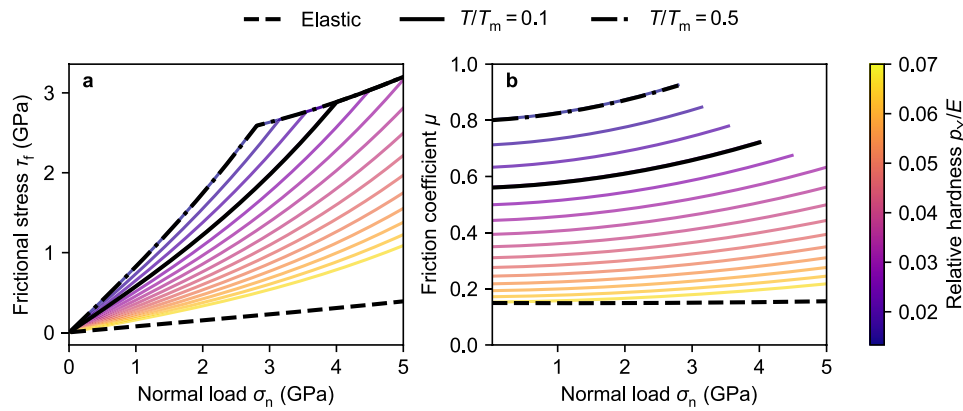


Fig. 12 Role of (temperature-dependent) hardness on frictional stress. **a** Frictional stress as a function of the normal load and hardness. The colored lines assume ideal plastic behavior with linear increase of the fractional contact area for different hardness to stiffness ratios. The elastic limit with real area of contact from Eq. (1) fitted to the elastic data in Fig. 9a is shown as a black dashed line. The solid line

represents friction for measured hardness at room temperature, and the dash-dotted line corresponds to a temperature-induced hardness reduction by 30% at 50% of the melting temperature, as estimated from literature data (see Fig. S3). **b** Same data as in **a**, but only the friction coefficient in the sliding regime is shown

that describes the hardness in the range of the data.¹ We selected three martensitic steel grades from their data with similar composition as AISI4140 but different levels of hardness. When normalized by the room temperature hardness H_{RT} , this data collapses to a single master curve, which can be described by the two empirical parameters A and B as shown in Fig. S3. Figure 12 shows the effect of the temperature correction on our friction model. In Fig. 12a, we plot the frictional shear stress over the macroscopic normal stress. The solid black line describes the friction based on room temperature hardness similar to the data shown in Fig. 10a, whereas the dashed black line is the elastic limit based on the Finnie and Shaw [12] model fitted to our elastic contact mechanics simulations. The dash-dotted black line assumes thermal softening at 50% of the melting temperature, which leads to a significant hardness reduction, and therefore higher friction in the sliding regime, with friction coefficients close to unity (see Fig. 12b). The colored lines further highlight the effect of hardness—be it due to temperature or steel grade—in the proposed friction model. If the ratio of hardness to Young’s modulus increases, the elastic limit is approached, but for metals at elevated temperatures, this limit is probably hard to reach.

The validation of the developed friction model by means of 2D FE simulation shows a good agreement with the executed experiments in terms of measured forces F_c and F_p , as well as the contact length l_c . The modeling of the friction between the tool and workpiece takes a major role to

accurately predict the cutting conditions in orthogonal cutting. It influences the predicted forces by up to 10% [72] but most significantly the contact length by up to 40% [16], and, therefore, the thermomechanical load at the contact zone formed between tool and chip [73]. Eventually, these loads affect the residual stresses of the machined layer [74].

The predicted friction coefficients are in the range of those found with conventional methods. However, care has to be taken, when interpreting the result due to the inherent model assumptions taken at the individual multiscale simulation steps. Those include for instance the selection of the tribofilm composition, the choice of the saturation hardness model, or the temperature dependence of the hardness. While an extensive parametrization of a composition-dependent shear stress model with DFTMD might be computationally too expensive, consideration of elasto-plastic contact beyond the saturation hardness could further improve our model. Our contact area calculations with the saturation hardness model are almost independent of the topography (cf. Bowden and Tabor), and thus, independent of the experimental resolution (see also Fig. S2). However, further enhancements of the plasticity model may depend on roughness and require surface characterization at higher resolution. Furthermore, a more detailed characterization of the formed tribofilms may enhance the atomistic models, and the friction model might be extended to include thermal effects beyond the hardness correction. In particular, the variation in thermal loads caused by different cutting conditions (cutting speed, chip thickness and rake angle) should be implemented into the friction model. Temperature measurements from experiments might be compared with the temperatures of the simulations with the temperature dependent friction model to improve our understanding of the cutting fluid’s

¹ We emphasize that this relation is solely empirical and lacks any physical interpretation. Note, that negative hardness would be possible at high temperatures. We made sure that this is not the case here.

role as a coolant. Furthermore, the plowing component of friction should be taken into account in order to represent a holistic friction law for cutting operations.

The overall good performance of the friction model, which was parametrized without experimental calibration on the cutting process itself, seems promising and may provide more accurate predictions for various cutting processes in the future. Including damage evolution into the FE simulations may further improve the prediction accuracy. Although it may not be feasible to create multiscale digital twins for a wide range of systems and cutting conditions, our results should be seen as a proof of concept for more physically motivated friction models in cutting simulations.

5 Conclusion

In this work, we have parametrized a friction model for the use in finite element (FE) cutting simulations of AISI4140 using a combination of experiments and numerical simulations on various scales. The severe thermomechanical loads during cutting usually do not allow parametrization based on analogous experiments, and therefore, friction models are usually parametrized using the cutting experiment itself. Here, we formulated a model similar to existing ones based on the real area of contact between rough surfaces and the stress required to shear adhesive micro contacts. Microtextured cutting tools and their negative imprint on the chips were used to orient chip and tool surfaces w.r.t each other, which led to the determination of a combined surface roughness between chip and tool. These effective rough topographies were then used in contact mechanics calculations with a penetration hardness model based on indentation hardness measurements of the chips. Due to their relative softness, in accordance with the Bowden and Tabor theory, the fractional contact area grows linearly with the applied normal load. The effective roughness of the tool chip surface topography pairs were found to be insensitive to the use of cutting fluid. The required shear stress as a function of the normal load has been calculated with DFT-based molecular dynamics simulations for a pseudo-amorphous tribofilm formed at the interface. The atomic composition of the film was inferred from *ex-situ* XPS depth profiling of the cutting tools, which contained mainly carbon, oxidized iron, and oxygen, next to the constituents of the ceramics coatings. When used in two-dimensional finite element chip forming simulations of an orthogonal cutting process, the results based on our friction model show a good agreement with experiments across a wide range of cutting conditions. On average, cutting and passive forces deviate approximately 5 and 11% from the experimental result, respectively, with few outliers under mild cutting conditions (low rake angle and uncut chip thickness). Equally promising results were found

for the prediction of the contact length, with an average deviation of less than 10%. Our work is a proof of concept for an alternative, physics-based calibration of constitutive models in metal cutting, and may provide a starting point for the use of more multiscale and multiphysical simulations in machining.

Supplementary Information The online version contains supplementary material available at <https://doi.org/10.1007/s11249-024-01906-9>.

Acknowledgements The authors gratefully acknowledge the funding of this work within the Priority Program 2231 “Efficient Cooling, Lubrication and Transport-Coupled Mechanical and Fluid Dynamic Simulation Methods for Efficient Production Processes (FLUSIM-PRO)” by the German Research Foundation (DFG)—Project no. SCHU 1010-2 and MO 879-2. The authors gratefully acknowledge the Gauss Centre for Supercomputing e.V. (<https://www.gauss-centre.eu>).

Author Contributions All authors contributed to the study conception and design. Material preparation, data collection and analysis were performed by H.H., F.S., P.B.G., L.M., and M.D. H.H. and F.S. wrote the first draft of the manuscript, and all authors commented on previous versions of the manuscript. All authors read and approved the final manuscript.

Funding Open Access funding enabled and organized by Projekt DEAL. This project by providing computing time through the John von Neumann Institute for Computing (NIC) on the GCS Supercomputer JUWELS at Jülich Supercomputing Centre (JSC).

Data Availability Surface topographies, contact mechanics setups, and results have been deposited on Zenodo and are available under the <https://doi.org/10.5281/zenodo.12610540>. Further raw data is available upon request to the corresponding authors.

Declarations

Conflict of Interest The authors declare no conflict of interest.

Open Access This article is licensed under a Creative Commons Attribution 4.0 International License, which permits use, sharing, adaptation, distribution and reproduction in any medium or format, as long as you give appropriate credit to the original author(s) and the source, provide a link to the Creative Commons licence, and indicate if changes were made. The images or other third party material in this article are included in the article’s Creative Commons licence, unless indicated otherwise in a credit line to the material. If material is not included in the article’s Creative Commons licence and your intended use is not permitted by statutory regulation or exceeds the permitted use, you will need to obtain permission directly from the copyright holder. To view a copy of this licence, visit <http://creativecommons.org/licenses/by/4.0/>.

References

1. Johnson, G.R., Cook, W.H.: A constitutive model and data for metals subjected to large strains, high strain rates and high temperatures. In: Proceedings of the 7th international symposium on ballistics, The Hague, Netherlands (1983)
2. Childs, T.H.C.: Friction modelling in metal cutting. *Wear* **260**(3), 310–318 (2006). <https://doi.org/10.1016/j.wear.2005.01.052>

3. Merchant, M.E.: Mechanics of the metal cutting process. II. Plasticity conditions in orthogonal cutting. *J. Appl. Phys.* **16**(6), 318–324 (1945). <https://doi.org/10.1063/1.1707596>
4. Lee, E.H., Shaffer, B.W.: The theory of plasticity applied to a problem of machining. *J. Appl. Mech.* **18**(4), 405–413 (1951). <https://doi.org/10.1115/1.4010357>
5. Li, B., Wang, X., Hu, Y., Li, C.: Analytical prediction of cutting forces in orthogonal cutting using unequal division shear-zone model. *Int. J. Adv. Manuf. Technol.* **54**(5), 431–443 (2011). <https://doi.org/10.1007/s00170-010-2940-8>
6. Zhou, F.: A new analytical tool-chip friction model in dry cutting. *Int. J. Adv. Manuf. Technol.* **70**(1), 309–319 (2014). <https://doi.org/10.1007/s00170-013-5271-8>
7. Bowden, F.P., Tabor, D.: Mechanism of metallic friction. *Nature* **150**(3798), 197–199 (1942). <https://doi.org/10.1038/150197a0>
8. Usui, E., Takeyama, H.: A photoelastic analysis of machining stresses. *J. Eng. Ind.* **82**(4), 303–307 (1960). <https://doi.org/10.1115/1.3664233>
9. Chandrasekaran, H., Kapoor, D.V.: Photoelastic analysis of tool-chip interface stresses. *J. Eng. Ind.* **87**(4), 495–502 (1965). <https://doi.org/10.1115/1.3670869>
10. Kato, S., Yamaguchi, K., Yamada, M.: Stress distribution at the interface between tool and chip in machining. *J. Eng. Ind.* **94**(2), 683–689 (1972). <https://doi.org/10.1115/1.3428229>
11. Childs, T.H.C., Mahdi, M.I., Barrow, G.: On the stress distribution between the chip and tool during metal turning. *CIRP Ann.* **38**(1), 55–58 (1989). [https://doi.org/10.1016/S0007-8506\(07\)62651-1](https://doi.org/10.1016/S0007-8506(07)62651-1)
12. Finnie, I., Shaw, M.C.: The friction process in metal cutting. *J. Fluids Eng.* **78**(8), 1649–1653 (1956). <https://doi.org/10.1115/1.4014128>
13. Shirakashi, T., Usui, E.: Friction characteristics on tool face in metal machining. *J. Jpn. Soc. Precis. Eng.* **39**(464), 966–972 (1973). <https://doi.org/10.2493/jjspe1933.39.966>
14. Dirikolu, M.H., Childs, T.H.C., Maekawa, K.: Finite element simulation of chip flow in metal machining. *Int. J. Mech. Sci.* **43**(11), 2699–2713 (2001). [https://doi.org/10.1016/S0020-7403\(01\)00047-9](https://doi.org/10.1016/S0020-7403(01)00047-9)
15. Zorev, N.N.: Inter-relationship between shear processes occurring along tool face and shear plane in metal cutting. *Int. Res. Product. Eng.* **49**, 143–152 (1963)
16. Özel, T.: The influence of friction models on finite element simulations of machining. *Int. J. Mach. Tools Manuf.* **46**(5), 518–530 (2006). <https://doi.org/10.1016/j.ijmactools.2005.07.001>
17. Zemzemi, F., Rech, J., Ben Salem, W., Dogui, A., Kapsa, P.: Identification of a friction model at tool/chip/workpiece interfaces in dry machining of AISI4142 treated steels. *J. Mater. Process. Technol.* **209**(8), 3978–3990 (2009). <https://doi.org/10.1016/j.jmatp.2008.09.019>
18. Rech, J., Claudin, C., D'Eramo, E.: Identification of a friction model—application to the context of dry cutting of an AISI 1045 annealed steel with a TiN-coated carbide tool. *Tribol. Int.* **42**(5), 738–744 (2009). <https://doi.org/10.1016/j.triboint.2008.10.007>
19. Smolenicki, D., Boos, J., Kuster, F., Roelofs, H., Wyen, C.F.: In-process measurement of friction coefficient in orthogonal cutting. *CIRP Ann.* **63**(1), 97–100 (2014). <https://doi.org/10.1016/j.cirp.2014.03.083>
20. Özel, T., Altan, T.: Determination of workpiece flow stress and friction at the chip-tool contact for high-speed cutting. *Int. J. Mach. Tools Manuf.* **40**(1), 133–152 (2000). [https://doi.org/10.1016/S0890-6955\(99\)00051-6](https://doi.org/10.1016/S0890-6955(99)00051-6)
21. Özel, T., Zeren, E.: A methodology to determine work material flow stress and tool-chip interfacial friction properties by using analysis of machining. *J. Manuf. Sci. Eng.* **128**(1), 119–129 (2005). <https://doi.org/10.1115/1.2118767>
22. Storchak, M., Rupp, P., Möhring, H.-C., Stehle, T.: Determination of Johnson-Cook constitutive parameters for cutting simulations. *Metals* **9**(4), 473 (2019). <https://doi.org/10.3390/met9040473>
23. Malakizadi, A., Hosseinkhani, K., Mariano, E., Ng, E., Del Prete, A., Nyborg, L.: Influence of friction models on FE simulation results of orthogonal cutting process. *Int. J. Adv. Manuf. Technol.* **88**(9–12), 3217–3232 (2017). <https://doi.org/10.1007/s00170-016-9023-4>
24. Ellersiek, L., Menze, C., Sauer, F., Denkena, B., Möhring, H.-C., Schulze, V.: Evaluation of methods for measuring tool-chip contact length in wet machining using different approaches (microtextured tool, in-situ visualization and restricted contact tool). *Prod. Eng. Res. Dev.* **16**(5), 635–646 (2022). <https://doi.org/10.1007/s11740-022-01127-w>
25. Sauer, F., Arndt, T., Schulze, V.: Tool wear development in gear skiving process of different quenched and tempered internal gears. *VDI **2389***, 1331–1343 (2022)
26. Openskiving (Version 1.62). KIT Campus Transfer GmbH (2024)
27. Virtanen, P., Gommers, R., Oliphant, T.E., Haberland, M., Reddy, T., Cournapeau, D., Burovski, E., Peterson, P., Weckesser, W., Bright, J., van der Walt, S.J., Brett, M., Wilson, J., Millman, K.J., Mayorov, N., Nelson, A.R.J., Jones, E., Kern, R., Larson, E., Carey, C.J., Polat, İ, Feng, Y., Moore, E.W., VanderPlas, J., Laxalde, D., Perktold, J., Cimrman, R., Henriksen, I., Quintero, E.A., Harris, C.R., Archibald, A.M., Ribeiro, A.H., Pedregosa, F., van Mulbregt, P.: SciPy 1.0 contributors: SciPy 1.0: fundamental algorithms for scientific computing in python. *Nat. Methods* **17**, 261–272 (2020). <https://doi.org/10.1038/s41592-019-0686-2>
28. Röttger, M.C., Sanner, A., Thimons, L.A., Junge, T., Gujrati, A., Monti, J.M., Nöhring, W.G., Jacobs, T.D.B., Pastewka, L.: Contact.engineering—create, analyze and publish digital surface twins from topography measurements across many scales. *Surf. Topogr.: Metrol. Prop.* **10**(3), 035032 (2022). <https://doi.org/10.1088/2051-672X/ac860a>
29. Fox-Rabinovich, G.S., Beake, B.D., Endrino, J.L., Veldhuis, S.C., Parkinson, R., Shuster, L.S., Migranov, M.S.: Effect of mechanical properties measured at room and elevated temperatures on the wear resistance of cutting tools with TiAlN and AlCrN coatings. *Surf. Coat. Technol.* **200**(20), 5738–5742 (2006). <https://doi.org/10.1016/j.surfcoat.2005.08.132>
30. Le Bourhis, E., Goudeau, P., Staia, M.H., Carrasquero, E., Puchi-Cabrera, E.S.: Mechanical properties of hard AlCrN-based coated substrates. *Surf. Coat. Technol.* **203**(19), 2961–2968 (2009). <https://doi.org/10.1016/j.surfcoat.2009.03.017>
31. Stanley, H.M., Kato, T.: An FFT-based method for rough surface contact. *J. Tribol.* **119**(3), 481–485 (1997). <https://doi.org/10.1115/1.2833523>
32. Polonsky, I.A., Keer, L.M.: A numerical method for solving rough contact problems based on the multi-level multi-summation and conjugate gradient techniques. *Wear* **231**(2), 206–219 (1999). [https://doi.org/10.1016/S0043-1648\(99\)00113-1](https://doi.org/10.1016/S0043-1648(99)00113-1)
33. Almqvist, A., Sahlin, F., Larsson, R., Glavatskih, S.: On the dry elasto-plastic contact of nominally flat surfaces. *Tribol. Int.* **40**(4), 574–579 (2007). <https://doi.org/10.1016/j.triboint.2005.11.008>
34. Weber, B., Suhina, T., Junge, T., Pastewka, L., Brouwer, A.M., Bonn, D.: Molecular probes reveal deviations from Amontons' law in multi-asperity frictional contacts. *Nat. Commun.* **9**(1), 888 (2018). <https://doi.org/10.1038/s41467-018-02981-y>
35. Frérot, L., Bonnet, M., Molinari, J.-F., Anciaux, G.: A Fourier-accelerated volume integral method for elastoplastic contact. *Comput. Methods Appl. Mech. Eng.* **351**, 951–976 (2019). <https://doi.org/10.1016/j.cma.2019.04.006>
36. Frérot, L., Anciaux, G., Rey, V., Pham-Ba, S., Molinari, J.-F.: Tamaas: a library for elastic-plastic contact of periodic rough

- surfaces. *J. Open Sour. Softw.* **5**(51), 2121 (2020). <https://doi.org/10.21105/joss.02121>
37. Frérot, L., Anciaux, G., Molinari, J.-F.: Crack nucleation in the adhesive wear of an elastic-plastic half-space. *J. Mech. Phys. Solids* **145**, 104100 (2020). <https://doi.org/10.1016/j.jmps.2020.104100>
 38. Larsen, A.H., Mortensen, J.J., Blomqvist, J., Castelli, I.E., Christensen, R., Duřak, M., Friis, J., Groves, M.N., Hammer, B., Hargus, C., Hermes, E.D., Jennings, P.C., Jensen, P.B., Kermode, J., Kitchin, J.R., Kolsbjerg, E.L., Kubal, J., Kaasbjerg, K., Lysgaard, S., Maronsson, J.B., Maxson, T., Olsen, T., Pastewka, L., Peterson, A., Rostgaard, C., Schiřt, J., Schiřt, O., Strange, M., Thygesen, K.S., Vegge, T., Vilhelmsen, L., Walter, M., Zeng, Z., Jacobsen, K.W.: The atomic simulation environment—a Python library for working with atoms. *J. Phys.: Condens. Matter* **29**(27), 273002 (2017). <https://doi.org/10.1088/1361-648X/aa680e>
 39. Kühne, T.D., Iannuzzi, M., Del Ben, M., Rybkin, V.V., Seewald, P., Stein, F., Laino, T., Khaliullin, R.Z., Schiřt, O., Schiffmann, F., Golze, D., Wilhelm, J., Chulkov, S., Bani-Hashemian, M.H., Weber, V., Borřtnik, U., Taillefumier, M., Jakobovits, A.S., Lazarro, A., Pabst, H., Müller, T., Schade, R., Guidon, M., Andermatt, S., Holmberg, N., Schenter, G.K., Hehn, A., Bussy, A., Belleflamme, F., Tabacchi, G., Glöß, A., Lass, M., Bethune, I., Mundy, C.J., Plessl, C., Watkins, M., VandeVondele, J., Krack, M., Hutter, J.: CP2K: an electronic structure and molecular dynamics software package—Quickstep: efficient and accurate electronic structure calculations. *J. Chem. Phys.* **152**(19), 194103 (2020). <https://doi.org/10.1063/5.0007045>
 40. Perdew, J.P., Burke, K., Ernzerhof, M.: Generalized gradient approximation made simple. *Phys. Rev. Lett.* **77**(18), 3865–3868 (1996). <https://doi.org/10.1103/PhysRevLett.77.3865>
 41. VandeVondele, J., Hutter, J.: Gaussian basis sets for accurate calculations on molecular systems in gas and condensed phases. *J. Chem. Phys.* **127**(11), 114105 (2007). <https://doi.org/10.1063/1.2770708>
 42. Goedecker, S., Teter, M., Hutter, J.: Separable dual-space Gaussian pseudopotentials. *Phys. Rev. B* **54**(3), 1703–1710 (1996). <https://doi.org/10.1103/PhysRevB.54.1703>
 43. MSC Marc (Version 2023.3). Hexagon AB (2024)
 44. Schwalm, J., Mann, F., González, G., Zanger, F., Schulze, V.: Finite element simulation of the process combination hammering turning. *Procedia CIRP* **117**, 110–115 (2023). <https://doi.org/10.1016/j.procir.2023.03.020>
 45. González, G., Sauer, F., Plogmeyer, M., Gerstenmeyer, M., Bräuer, G., Schulze, V.: Effect of thermomechanical loads and nanocrystalline layer formation on induced surface hardening during orthogonal cutting of AISI 4140. *Procedia CIRP* **108**, 228–233 (2022). <https://doi.org/10.1016/j.procir.2022.03.040>
 46. Sauer, F., Codrignani, A., Haber, M., Falk, K., Mayrhofer, L., Schwitzke, C., Moseler, M., Bauer, H.-J., Schulze, V.: Multi-scale simulation approach to predict the penetration depth of oil between chip and tool during orthogonal cutting of AISI 4140. *Procedia CIRP* **117**, 426–431 (2023). <https://doi.org/10.1016/j.procir.2023.03.072>
 47. Stampfer, B., González, G., Segebade, E., Gerstenmeyer, M., Schulze, V.: Material parameter optimization for orthogonal cutting simulations of AISI4140 at various tempering conditions. *Procedia CIRP* **102**, 198–203 (2021). <https://doi.org/10.1016/j.procir.2021.09.034>
 48. Richter, F.: Die physikalischen Eigenschaften der Stähle—Das 100-Stähle-Programm. Tafeln und Bilder, Teil I (2015)
 49. Agmell, M., Ahadi, A., Stähel, J.-E.: A fully coupled thermomechanical two-dimensional simulation model for orthogonal cutting: Formulation and simulation. *Proc. Inst. Mech. Eng., Part B: J. Eng. Manuf.* **225**(10), 1735–1745 (2011). <https://doi.org/10.1177/0954405411407137>
 50. Sarmiento, G.S., Bugna, J.F., Canale, L.C.F., Riofano, R.M.M., Mesquita, R.A., Totten, G.E., Canale, A.C.: Modeling quenching performance by the Kuyucak method. *Mater. Sci. Eng., A* **459**(1), 383–389 (2007). <https://doi.org/10.1016/j.msea.2007.01.025>
 51. Kops, L., Arenson, M.: Determination of convective cooling conditions in turning. *CIRP Ann.* **48**(1), 47–52 (1999). [https://doi.org/10.1016/S0007-8506\(07\)63129-1](https://doi.org/10.1016/S0007-8506(07)63129-1)
 52. Bowden, F.P., Tabor, D., Taylor, G.I.: The area of contact between stationary and moving surfaces. *Proc. R. Soc. Lond. Ser. A. Math. Phys. Sci.* **169**(938), 391–413 (1939). <https://doi.org/10.1098/rspa.1939.0005>
 53. Xie, J., Luo, M.-J., He, J.-L., Liu, X.-R., Tan, T.-W.: Micro-grinding of micro-groove array on tool rake surface for dry cutting of titanium alloy. *Int. J. Precis. Eng. Manuf.* **13**(10), 1845–1852 (2012). <https://doi.org/10.1007/s12541-012-0242-9>
 54. Kümmel, J., Braun, D., Gibmeier, J., Schneider, J., Greiner, C., Schulze, V., Wanner, A.: Study on micro texturing of uncoated cemented carbide cutting tools for wear improvement and built-up edge stabilisation. *J. Mater. Process. Technol.* **215**, 62–70 (2015). <https://doi.org/10.1016/j.jmatprotec.2014.07.032>
 55. Obikawa, T., Kamio, A., Takaoka, H., Osada, A.: Micro-texture at the coated tool face for high performance cutting. *Int. J. Mach. Tools Manuf.* **51**(12), 966–972 (2011). <https://doi.org/10.1016/j.ijmactools.2011.08.013>
 56. Kang, Z., Fu, Y., Ji, J., Tian, L.: Numerical investigation of microtexture cutting tool on hydrodynamic lubrication. *J. Tribol.* **139**(5), 054502 (2017). <https://doi.org/10.1115/1.4035506>
 57. Sanner, A., Nöhrling, W.G., Thimons, L.A., Jacobs, T.D.B., Pastewka, L.: Scale-dependent roughness parameters for topography analysis. *Appl. Surf. Sci. Adv.* **7**, 100190 (2022). <https://doi.org/10.1016/j.apsadv.2021.100190>
 58. Persson, B.N.J.: Elastoplastic contact between randomly rough surfaces. *Phys. Rev. Lett.* **87**(11), 116101 (2001). <https://doi.org/10.1103/PhysRevLett.87.116101>
 59. Persson, B.N.J.: Theory of rubber friction and contact mechanics. *J. Chem. Phys.* **115**(8), 3840–3861 (2001). <https://doi.org/10.1063/1.1388626>
 60. Erdemir, A., Eryilmaz, O.L., Fenske, G.: Synthesis of diamondlike carbon films with superlow friction and wear properties. *J. Vac. Sci. Technol., A: Vac., Surf. Films* **18**(4 II), 1987–1992 (2000). <https://doi.org/10.1116/1.582459>
 61. Robertson, J.: Diamond-like amorphous carbon. *Mater. Sci. Eng. R. Rep.* **37**(4), 129–281 (2002). [https://doi.org/10.1016/S0927-796X\(02\)00005-0](https://doi.org/10.1016/S0927-796X(02)00005-0)
 62. Argibay, N., Babuska, T.F., Curry, J.F., Dugger, M.T., Lu, P., Adams, D.P., Nation, B.L., Doyle, B.L., Pham, M., Pimentel, A., Mowry, C., Hinkle, A.R., Chandross, M.: In-situ tribochemical formation of self-lubricating diamond-like carbon films. *Carbon* **138**, 61–68 (2018). <https://doi.org/10.1016/j.carbon.2018.06.006>
 63. Aizawa, T., Mitsuo, A., Yamamoto, S., Sumitomo, T., Muraishi, S.: Self-lubrication mechanism via the in situ formed lubricious oxide tribofilm. *Wear* **259**(1), 708–718 (2005). <https://doi.org/10.1016/j.wear.2005.02.025>
 64. Sumitomo, T., Aizawa, T., Yamamoto, S.: In-situ formation of self-lubricating tribo-films for dry machinability. *Surf. Coat. Technol.* **200**(5), 1797–1803 (2005). <https://doi.org/10.1016/j.surfcoat.2005.08.055>
 65. Podchernyaeva, I.A., Klimenko, S.A., Beresnev, V.M., Panashenko, V.M., Toryanik, I.N., Klimenko, S.A., Kopeikina, M.Y.: Formation of a tribofilm in the surface layer of Al–Ti–Cr–N–B magnetron coating on boron nitride during turning of hardened steel. *Powder Metall. Met. Ceram.* **54**(3–4), 140–150 (2015). <https://doi.org/10.1007/s11106-015-9691-x>
 66. Yuan, J., Fox-Rabinovich, G.S., Veldhuis, S.C.: Control of tribofilm formation in dry machining of hardened AISI D2 steel by

- tuning the cutting speed. *Wear* **402–403**, 30–37 (2018). <https://doi.org/10.1016/j.wear.2018.01.015>
67. Arrazola, P.J., Arriola, I., Davies, M.A., Cooke, A.L., Dutterer, B.S.: The effect of machinability on thermal fields in orthogonal cutting of AISI 4140 steel. *CIRP Ann.* **57**(1), 65–68 (2008). <https://doi.org/10.1016/j.cirp.2008.03.139>
68. Cakir, E., Ozlu, E., Bakkal, M., Budak, E.: Investigation of temperature distribution in orthogonal cutting through dual-zone contact model on the rake face. *Int. J. Adv. Manuf. Technol.* **96**(1), 81–89 (2018). <https://doi.org/10.1007/s00170-017-1479-3>
69. Li, T., Shi, T., Tang, Z., Liao, G., Han, J., Duan, J.: Temperature monitoring of the tool-chip interface for PCBN tools using built-in thin-film thermocouples in turning of titanium alloy. *J. Mater. Process. Technol.* **275**, 116376 (2020). <https://doi.org/10.1016/j.jmatprotec.2019.116376>
70. Merchant, H.D., Murty, G.S., Bahadur, S.N., Dwivedi, L.T., Mehrotra, Y.: Hardness-temperature relationships in metals. *J. Mater. Sci.* **8**(3), 437–442 (1973). <https://doi.org/10.1007/BF00550166>
71. Torres, H., Varga, M., Ripoll, M.R.: High temperature hardness of steels and iron-based alloys. *Mater. Sci. Eng., A* **671**, 170–181 (2016). <https://doi.org/10.1016/j.msea.2016.06.058>
72. Bil, H., Kılıç, S.E., Tekkaya, A.E.: A comparison of orthogonal cutting data from experiments with three different finite element models. *Int. J. Mach. Tools Manuf.* **44**(9), 933–944 (2004). <https://doi.org/10.1016/j.ijmachtools.2004.01.016>
73. Shi, G., Deng, X., Shet, C.: A finite element study of the effect of friction in orthogonal metal cutting. *Finite Elem. Anal. Des.* **38**(9), 863–883 (2002). [https://doi.org/10.1016/S0168-874X\(01\)00110-X](https://doi.org/10.1016/S0168-874X(01)00110-X)
74. Liu, C.R., Guo, Y.B.: Finite element analysis of the effect of sequential cuts and tool-chip friction on residual stresses in a machined layer. *Int. J. Mech. Sci.* **42**(6), 1069–1086 (2000). [https://doi.org/10.1016/S0020-7403\(99\)00042-9](https://doi.org/10.1016/S0020-7403(99)00042-9)

Publisher's Note Springer Nature remains neutral with regard to jurisdictional claims in published maps and institutional affiliations.